Published in final edited form as:
Magn Reson Med. 2012 February ; 67(2): 428–436. doi:10.1002/mrm.23026.

Short TE 3D Radial Gradient-Echo MRI Using Concurrent Dephasing and Excitation (CODE)

Jang-Yeon Park[1,2,*], **Steen Moeller**[2], **Ute Goerke**[2], **Edward Auerbach**[2], **Ryan Chamberlain**[2], **Jutta Ellermann**[2], and **Michael Garwood**[2]

[1]School of Biomedical Engineering, College of Biomedical and Health Science, Research Institute of Biomedical Engineering, Konkuk University, Chungju, Korea (ROK)

[2]The Center for Magnetic Resonance Research and Department of Radiology, University of Minnesota Medical School, Minneapolis, Minnesota, USA

Abstract

Ultrashort echo time (UTE) imaging and sweep imaging with Fourier transformation (SWIFT) are powerful techniques developed for imaging ultrashort T_2 species. However, it can be challenging to implement them on standard clinical MRI systems due to demanding hardware requirements. In this paper the limits of what is possible in terms of the minimum echo time (*TE*) and repetition time (*TR*) with 3D radial gradient-echo (GRE) sequences, which can be readily implemented on a standard clinical scanner, are investigated. In addition, a new 3D radial GRE sequence is introduced, called CODE (COncurrent Dephasing and Excitation). The unique feature of CODE is that the initial dephasing of the readout gradient is performed during RF excitation, which allows CODE to effectively achieve echo times on the order of ~0.2 ms and larger in a clinical setting. The minimum *TE* achievable with CODE is analytically described and compared with a standard 3D radial GRE sequence. CODE was implemented on a clinical 3T scanner (Siemens 3T MAGNETOM Trio), and both phantom and *in vivo* human knee images are shown for demonstration.

Keywords

UTE imaging; 3D radial gradient-echo imaging; CODE; radial sampling; short TE; short TR

INTRODUCTION

Recently, multiple subspecialty areas of MRI research have experienced a surge of interest in techniques to image spins with very short transverse relaxation times, T_2 and T_2*. For biomedical MRI, the musculoskeletal system in particular contains a majority of short T_2 components in connective tissues such as cortical and trabecular bone, meniscal and labral tissues, ligaments and tendons. Such tissues are not easily detected with conventional MRI sequences. Hence, methods like ultrashort echo-time (UTE) imaging (1,2) and sweep imaging with Fourier transformation (SWIFT) (3,4) have been developed to image tissue water signals with T_2 components as short as 100 – 200 μs. With gradient-recalled echo (GRE) imaging, it is generally assumed that the shortest achievable echo time (*TE*) is ~2 ms when imaging with a clinical scanner. With UTE and SWIFT on the other hand, the delay

*Address correspondence to: Jang-Yeon Park, Ph.D., School of Biomedical Engineering, Konkuk University, Danwol-dong 322, Chungju-si, Chungcheongbuk-do, 380-701, Korea Phone: 82-43-840-3761, Fax: 82-43-851-0620, jyparu@kku.ac.kr.

Presented in part at the ISMRM meetings in Seattle, USA, 2006 and Berlin, Germany, 2007.

(or dead time) between excitation and the start of signal acquisition is made very short by acquiring a free induction decay (FID) instead of a gradient-recalled echo. One point worth mentioning here is that the common use of *TE* to describe the delay between excitation and FID acquisition is inconsistently defined. We therefore prefer to use the alternative terminology of "acquisition delay" in the description of UTE and SWIFT.

In both UTE and SWIFT, *k*-space is filled in a radial manner (i.e., with "spokes" radiating out from $k = 0$). In UTE imaging, after radiofrequency (RF) excitation, data acquisition begins as quickly as possible while the readout gradient is being ramped on, to minimize signal loss and blurring (5). To capture signals from extremely short T_2 spins, UTE is typically implemented with a short RF pulse (which usually necessitates high peak RF amplitude, B_1^{max}) and high gradient slew rate. The shortest achievable acquisition delay is ~ 20 – 100 μs on most clinical scanners, although ~ 8 μs is the shortest acquisition delay that has been reported (6). UTE also encounters challenges relating to non-uniform sampling as a result of sampling data on the gradient ramp. Gridding of non-uniformly acquired data in *k*-space is particularly difficult since the gradient ramp is not perfectly linear in many cases and the gradients on different axes can have different temporal responses (7). In SWIFT, the gradient field is constant while acquiring the data in a time-shared manner with the RF excitation. That is, the gradient amplitude is at a constant value while signal is acquired in gaps inserted in a broadband frequency-swept excitation pulse. The acquisition delay is limited only by the time needed for the coil ring down (and up) and to switch between transmit and receive modes. This time can be as short as 2 μs when using the latest electronic components in transmit/receive switches (in single transmit/receive coil configuration) or in pin-diode switches (in separate transmit/receive coil applications).

As a modified version of UTE imaging, water- and fat-suppressed projection MR imaging (WASPI) was also proposed in which the gradient is ramped on prior to the RF pulse and held constant until FID sampling is complete (8). In WASPI and related techniques (9,10), unlike UTE, data is acquired not on the gradient ramp, but on the constant gradient, avoiding the challenging problem of non-uniform sampling. However, since WASPI employs a non-selective square RF pulse in the presence of the gradient, the pulse length has to be very short to minimize the signal variation across the object, due to the sinc-shaped excitation profile of the square pulse. As a result, the requirement for high peak RF (B_1^{max}) can be more of a limitation for these techniques than for UTE and SWIFT. In addition, due to the FID sampling with a very fast rate (typically, 5 - 25 μs per point), data points close to the origin of *k*-space are not measured during the dead time of the receiver, and thus, an additional short data collection is sometimes needed to recover the lost points (11-13).

Both UTE and SWIFT rely on achieving superior hardware performance, and as a result, are currently undergoing intense development and testing in many different laboratories. For these reasons, standardized versions of these sequences are not yet widely available on commercial MRI scanners. Many applications, including musculoskeletal studies of tendons, ligaments, and meniscus, require detection of spins with T_2 values only in the 1 – 10 ms range, rather than in the tens to hundreds of microsecond range. In such cases, a GRE sequence using the shortest possible TE may suffice.

The purpose of the present study was therefore to investigate the limits of what is possible in terms of minimum *TE* and repetition time (*TR*) with 3D radial GRE imaging using a standard clinical scanner. In addition, a new 3D radial GRE sequence is introduced, called CODE (COncurrent Dephasing and Excitation). As can be recognized from its name, the unique feature of CODE is that the initial dephasing of the readout gradient is performed during RF excitation, which allows CODE to effectively achieve $TE \geq \sim 0.2$ ms on a clinical scanner. In this article, the minimum *TE* and *TR* achievable with CODE are analytically

described and compared with the more standard 3D radial GRE sequence (rGRE). It is also shown that CODE can be implemented on a clinical 3T scanner, and both phantom and *in vivo* human knee images are shown for demonstration.

METHODS

Pulse sequence and data acquisition

Simplified schematic diagrams of 3D UTE, rGRE, and CODE sequences are shown in Fig. 1. In UTE (Fig. 1a) and rGRE (Fig. 1b), a non-selective square pulse is used for spin excitation, whereas in CODE (Fig. 1c), a shaped pulse is needed to excite a relatively uniform flip angle in the presence of a slab-select gradient (G_{ss}). The essential feature of the UTE technique is that the FID acquisition begins while ramping up the readout gradient (G_{ro}) to achieve the shortest possible acquisition delay, without applying an initial dephasing (or pre-dephasing) gradient. Conversely, in rGRE and CODE, immediately following a pre-dephasing gradient which has the opposite polarity of G_{ro}, a gradient echo is acquired after the readout gradient has reached a plateau. The unique feature of CODE, however, is that slab selection and pre-dephasing are performed with the same gradient. In other words, a pre-dephasing gradient for the frequency-encoded readout is applied during, not after, spin excitation in CODE. Following excitation, acquisition is delayed only by the need to ramp the gradient in one direction, which allows the minimum *TE* to be less than that of rGRE. In CODE, a frequency-selective RF pulse such as a sinc or a hyperbolic secant pulse (sech/tanh) can be used for the spin excitation in the presence of the slab-select gradient, provided that the thickness of the selected slab is wider than the largest dimension of the object being imaged.

In rGRE and CODE, a partial gradient echo acquisition is exploited to minimize *TE*. The gradient ramps in the *x*, *y*, and *z* axes are required to have the same ramp time (τ) so that the gradients in these axes can start at the same time despite their different amplitudes and thus different rise times. The achievable minimum τ depends on the performance of a gradient system and, in CODE, is equal to the sum of the minimum τ of G_{ss} and G_{ro} (Fig. 1c). Here the minimum τ of G_{ss} and G_{ro} is given by dividing G_{ss} and G_{ro} by the maximum slew rate (*SR*), respectively. The radial sampling is typically performed with an isotropic angular spacing to cover a sphere in *k*-space, where the end of the spoke follows a spiral path on the surface of the sphere referred to as view orders (14). Several view-order spirals can be interleaved to increase the total number of projections.

When imaging short T_2 spins with CODE, the pulse length (T_p) is kept as short as possible to achieve the shortest *TE* within permissible B_1^{max} and specific absorption rate (SAR) constraints. In the usual implementation of CODE for human studies, T_p is typically ~100 - 300 microseconds, while the acquisition time (T_{acq}) is much longer, on the order of a few milliseconds or less, depending on the resolution and acquisition bandwidth. In this $T_p << T_{acq}$ case, the peak of the gradient echo forms soon after the start of the acquisition period. As a result, the gradient echoes used to fill *k*-space in each radial direction (i.e., the spokes) are asymmetric about the origin of *k*-space. Due to the asymmetric feature of the gradient-echoes, the highest spatial resolution achieved with rGRE and CODE is given by $FOV / \{2(n_{acq} - n_{short}) - 1\}$, where *FOV* is the field-of-view, n_{acq} is the number of sampled *k*-space points in data acquisition, n_{short} is the number of sampled points on the short side of the asymmetric echo.

In the current implementation of rGRE and CODE, images are reconstructed offline using gridding and fast Fourier transformation (FFT). Gridding is performed to distribute the radially sampled data onto Cartesian coordinates by convolving with a Kaiser-Bessel function for interpolation. Then 3D FFT is performed, followed by deapodization which

removes the interpolation effect caused by the gridding. For density correction in the gridding process, a two-step iterative gridding/regridding of ones is performed as proposed by Pipe *et al*. (15). To assign each measurement value to its correct *k*-space location, each channel was phased separately. Using the phase of the average projection, a single linear function was fitted in a weighted least-squares manner, where the weight was the magnitude of the average projection. From the slope of the linear function, the correct timing of *k*-space was determined.

The minimum *TE* achievable with CODE

In this section, the conditions for achieving the shortest *TE* with CODE are analyzed. For convenience, the slab thickness (*THK*) is assumed to be the same as the *FOV*. Under this assumption, the pulse bandwidth (*BW*) and the acquisition bandwidth (*SW*) are linearly proportional only to the magnitude of G_{ss} and G_{ro}, respectively. In this case, three different situations are considered for the analysis of the shortest *TE* achievable with CODE, which are: $BW > SW$ (or $G_{ss} > G_{ro}$), $BW = SW$ (or $G_{ss} = G_{ro}$), and $BW < SW$ (or $G_{ss} < G_{ro}$). These are referred to as case 1, 2, and 3, respectively.

To begin, let us compare case 1 (Fig. 2a) with case 2 (Fig. 2b) in terms of achievable minimum *TE*. With *TE* defined as the time between the center of the RF pulse and the peak of the echo, in cases 1 and 2,

$$TE_{CODE}=0.5T_p+\tau_{ss}+\tau_{ro}+T_{short}, \quad [1]$$

where T_{short} is the duration of the short-side of the asymmetric echo, τ_{ss} is the ramp time needed for G_{ss} to reach a plateau (= G_{ss}/SR), and τ_{ro} is the ramp time needed for G_{ro} to reach a plateau (= G_{ro}/SR). Provided that T_p, *SW*, and *FOV* are the same in the two cases, $TE_1 > TE_2$ because $\tau_{ss,1} > \tau_{ss,2}$ and $T_{short,1} > T_{short,2}$, where subscripts 1 and 2 indicate the case. Here, $\tau_{ss,1} > \tau_{ss,2}$ because $BW_1 > SW = BW_2$, and thus, $G_{ss,1} > G_{ss,2}$. $T_{short,1} > T_{short,2}$ can be inferred from the fact that the gradient area with respect to time for pre-dephasing in case 1 is greater than that in case 2, i.e., $G_{ss,1}(T_p/2 + \tau_{ss,1}) > G_{ss,2}(T_p/2 + \tau_{ss,2})$. Therefore, it is concluded that case 2 always offers a shorter *TE* than case 1.

In case 3, the gradient area for the pre-dephasing is less than that for the readout, and as a result additional time for dephasing with G_{ss} is needed to keep the echo peak from occurring during the readout gradient ramp. As shown in Figs. 2c and 2d, two sequence schemes are possible for this purpose. In the case of the basic scheme (Fig. 2c), which will be referred to as case 3a, G_{ss} is simply extended in time using the same (constant) G_{ss} value. However, in case 3b (Fig. 2d), a part of the extended gradient is replaced with gradient ramps (i.e., ramp-up and ramp-down) with an area (shaded triangle) equal to that of the part of the extended gradient to be replaced (shaded rectangle). Case 3b always provides a shorter *TE* than case 3a by the amount of time corresponding to the width of the shaded rectangle.

Now let us compare case 2 with case 3a. While TE_2 is given by Eq. [1], TE_{3a} is given by adding the extended dephasing time (τ_{ext}) to Eq. [1]. Provided that T_p, *SW*, and *FOV* (= *THK*) are the same in the two cases,

$$TE_2=0.5T_p+\tau_{ss,2}+\tau_{ro}+T_{short,2}, \quad [2]$$

$$TE_{3a}=0.5T_p+\tau_{ext}+\tau_{ss,3a}+\tau_{ro}+T_{short,3}, \quad [3]$$

where $T_{p,2} = T_{p,3} = T_p$ and $\tau_{ro,2} = \tau_{ro,3} = \tau_{ro}$. In Eq. [3], when it is also assumed that $T_{short,2} = T_{short,3}$, τ_{ext} can be expressed in terms of T_p and $\tau_{ss,2}$ by considering that the gradient area (A) for the predephasing in case 3a has to be equal to that in case 2, i.e., $A_2 = A_3$. For convenience, $\tau_{ss,3a}$ can be assumed to be $\alpha\tau_{ss,2}$, where $0 < \alpha < 1$, because $BW_3 > BW_2$ and thus, $G_{ss,3} > G_{ss,2}$. In this case, the expression for τ_{ext} in terms of T_p and $\tau_{ss,2}$ is obtained from the equation $A_2 = A_3$, which is,

$$\tau_{ext}=\frac{1-\alpha}{2\alpha}T_p+\frac{1-\alpha^2}{2\alpha}\tau_{ss,2}. \quad [4]$$

When using Eqs. [2], [3], and [4], the numerical difference between TE_{3a} and TE_2 is also given in terms of α, T_p, and $\tau_{ss,2}$,

$$\Delta TE_{3a}=TE_{3a}-TE_2=\tau_{ext}+\tau_{ss,3}-\tau_{ss,2}=\tau_{ext}+(\alpha-1)\,\tau_{ss,2}=\frac{1-\alpha}{2\alpha}T_p+\frac{(\alpha-1)^2}{2\alpha}\tau_{ss,2}. \quad [5]$$

Since both first and second terms in Eq. [5] are always positive due to the assumption that $0 < \alpha < 1$, TE_{3a} is always greater than TE_2, and thus, it is concluded that case 2 always provides a shorter TE than case 3a.

Next, let us compare case 2 with case 3b in which a part of the extended G_{ss} is replaced with gradient ramps. As shown in Fig. 2d, TE_{3b} is shorter than TE_{3a} by $\tau_{ss,3a}$. Thus, TE_{3b} is obtained by simply subtracting $\tau_{ss,3a}$ from Eq. [3],

$$TE_{3b}=0.5T_p+\tau_{ext}+\tau_{ro}+T_{short,3}. \quad [6]$$

In this case, the numerical difference between TE_{3b} and TE_2 is given by

$$\Delta TE_{3b}=TE_{3b}-TE_2=\tau_{ext}-\tau_{ss,2}=\frac{1-\alpha}{2\alpha}T_p+\frac{1-2\alpha-\alpha^2}{2\alpha}\tau_{ss,2}, \quad [7]$$

using Eqs. [2], [4], and [6]. Unlike ΔTE_{3a} in Eq. [5], ΔTE_{3b} is not always positive, which means that TE_{3b} is shorter than TE_2 in some cases. When determining the condition for $\Delta TE_{3b} > 0$, the constraint needs to be considered that τ_{ext} should be no less than $2\tau_{ss,3a}$ in order for the gradient ramp not to begin during the slab-selective excitation, i.e., $\tau_{ext} \geq 2\tau_{ss,3a}$ ($=\alpha\tau_{ss,2}$). Because the analysis for ΔTE_{3b} is complicated and tedious, let us go directly to the conclusion without presenting the detailed description of it here: For α larger than 0.5 (i.e., $0.5 < \alpha < 1$), case 2 always provides a shorter TE than case 3b. For α smaller than 0.5 (i.e., $0 < \alpha < 0.5$), case 2 provides a shorter TE than case 3b when $T_p > 0.5\tau_{ss,2}$, which occurs in human applications using a large THK. In the event that $T_p < 0.5\tau_{ss,2}$, which can be the case in animal studies (e.g., $THK \leq 5.2$ cm when $T_p = 0.1$ ms, $BW = 10$ kHz, and $SR = 170$ mT/m/ms), case 3b provides a shorter TE than case 2 for $\alpha_i < \alpha < 0.5$, where α_i is the point at which $\Delta TE_{3b} = 0$. In summary, case 2 provides the shortest TE achievable with CODE, except for case 3b when $T_p < 0.5\tau_{ss,2}$ for $\alpha_i < \alpha < 0.5$.

In Table 1, the minimum TE values and maximum flip angles achieved with CODE on a 3T Siemens Trio scanner are provided using a knee coil and a body coil. A sinc pulse was used with $R = 10$, where R is defined as the product of T_p and BW (i.e., $R = T_p \cdot BW$). n_{short} was set to be 4. The Siemens phantom D170 with distilled water (including 8.2g $NaC_2H_2O_2$ + 9.6g $C_3H_3O_3Li$ per 1000g H_2O) was used for coil loading. The minimum TE values were

measured for two different *FOV*s (25 cm and 40 cm), using different T_p values ranging from 0.1 - 0.25 ms in 0.05 ms increments. With T_p = 0.1 ms, the achievable minimum *TE* was 0.22 ms and 0.18 ms for *FOV* = 25 cm and 40 cm, respectively, and these were 0.31 ms and 0.27 ms with T_p = 0.25 ms. The maximum flip angles were also measured using the two coils. When using the knee coil, the maximum flip angle was 6° and 12° with T_p = 0.1 ms and 0.25 ms, respectively, and these were 3° and 9° for the body coil. As seen here, when a very short *TE* is needed, large flip angles cannot be attained with CODE due to the peak B_1 or SAR limitation.

The minimum *TE* achievable with rGRE

In the rGRE sequence (Fig. 1b), spins are excited by a short square pulse which is not slab selective (G_{ss} = 0), followed by a pre-dephasing gradient (G_{deph}), and then by G_{ro}. In order to minimize *TE*, the pre-dephasing gradient can be replaced by gradient ramps only (i.e., ramp up and ramp down) without a gradient plateau. In this case, the minimum *TE* is given by

$$TE_{rGRE}=T_p/2+2\tau_{depth}+\tau_{ro}+T_{short}, \quad [8]$$

where τ_{deph} is the ramp time for the pre-dephasing gradient to reach a setup value ($\tau_{deph} = G_{deph}/SR$). In the following section, the equations above will be analyzed in detail to determine which sequence, rGRE or CODE, affords the shortest *TE* values.

Comparison of the minimum *TE* between CODE and rGRE

Here, it is assumed that peak B_1 or SAR determines the minimum T_p. Hence, in the following comparison of CODE and rGRE, B_1^{max} or SAR is set equal in the two sequences and set to produce the same flip angle. Under these conditions, the duration of the square pulse used in rGRE will be shorter than that of the frequency-selective pulse (e.g., a sinc) used in CODE. Thus, it is reasonable to assume that the pulse lengths in CODE and rGRE are T_p and cT_p, respectively, where *c* is the ratio of the pulse length in these two sequences, whereby $0 < c \leq 1$. All the readout parameters such as *SW*, *FOV*, τ_{ro}, and T_{short} are also assumed to have the same values in both CODE and rGRE.

For the comparison of the minimum *TE* achievable with CODE (Eq. [1]) and rGRE (Eq. [8]), it is convenient to describe τ_{deph} in Eq. [8] in terms of τ_{ro} and T_{short}, considering that the gradient area of the dephasing (A_{deph}) is equal to that of the rephasing (A_{reph}). Given $\tau_{deph} = G_{deph}/SR$,

$$A_{deph}=\tau_{deph}\cdot G_{deph}=\left(\tau_{deph}\right)^2\cdot SR. \quad [9]$$

On the other hand, A_{reph} is given by the sum of the area of the gradient ramp and the readout gradient corresponding to T_{short}, which is,

$$A_{reph}=0.5\tau_{ro}\cdot G_{ro}+T_{short}\cdot G_{ro}=0.5(\tau_{ro})^2\cdot SR+T_{short}\cdot\tau_{ro}\cdot SR. \quad [10]$$

Given $A_{deph} = A_{reph}$ (i.e., Eq. [9] = Eq. [10]), τ_{deph} can be expressed as

$$\tau_{deph}=\left[0.5(\tau_{ro})^2+T_{short}\cdot\tau_{ro}\right]^{1/2}. \quad [11]$$

Using Eq. [11] and recalling that the pulse length in rGRE was assumed to be cT_p, the minimum *TE* achievable with rGRE (Eq. [8]) is rewritten as

$$TE_{rGRE}=0.5\left(cT_p\right)+2\left[0.5(\tau_{ro})^2+T_{short}\cdot\tau_{ro}\right]^{1/2}+\tau_{ro}+T_{short}. \quad [12]$$

As proven in the previous section, the minimum *TE* in CODE in most human applications is accomplished with case 2, i.e., when $BW = SW$. In this case, $\tau_{ss} = \tau_{ro}$, and thus, the minimum *TE* in CODE (Eq. [1]) can also be rewritten as

$$TE_{CODE}=0.5T_p+2\tau_{ro}+T_{short}. \quad [13]$$

From Eqs. [12] and [13], the condition can be derived for which $TE_{rGRE} = TE_{CODE}$. A quadratic equation in terms of τ_{ro} is obtained by using the fact that Eq. [12] = Eq. [13], which is,

$$(\tau_{ro})^2+\left[4T_{short}-(1-c)\,T_p\right]\cdot\tau_{ro}-0.25(1-c)^2\left(T_p\right)^2=0. \quad [14]$$

Since $T_{short} = T_p/2$ in CODE (i.e., in case 2), the coefficient of the second term in Eq. [14] is also expressed in terms of c and T_p. Hence, Eq. [14] is rewritten as

$$(\tau_{ro})^2+(1+C)\,T_p\cdot\tau_{ro}-0.25(1-c)^2\left(T_p\right)^2=0. \quad [15]$$

Eq. [15] has two real solutions and its non-trivial solution is

$$\tau_{ro}=0.5T_p\left[-1-c+\left(2+2c^2\right)^{1/2}\right]. \quad [16]$$

Since $\tau_{ro} = G_{ro}/SR = SW/(\gamma FOV\cdot SR)$, the condition for $TE_{CODE} < TE_{rGRE}$ is

$$SW>0.5\gamma FOV\cdot SR\cdot T_p\left[-1-c+\left(2+2c^2\right)^{1/2}\right], \quad [17]$$

where γ is the gyromagnetic ratio. In Fig. 3a, *SW* is plotted as a function of c (= $T_{p,rGRE}/T_{p,CODE}$) for different *FOV* values (= 20, 25, and 30 cm), as c varies between 0 and 1. CODE achieves a shorter *TE* than rGRE, provided that *SW* is larger than the plotted value for a given c; that is, when Eq. [17] is satisfied.

Table 2 provides examples of the minimum *TE* and *TR* achievable with CODE and rGRE for two different *FOV*s. For the calculation, a square pulse was used for rGRE and a standard sinc pulse with 3 lobes (R = 10) was used for CODE. The slew rate was set equal to that achievable with a 3T Siemens MAGNETOM Trio system (gradient slew rate = 170 mT/m/ms). A spoiling gradient was not considered for the calculation of *TR*. A maximum value of 500 Hz was assumed for $\gamma B_1/2\pi$, which is a readily attainable value with a whole-body RF coil. The flip angle was set to 3.9° in both pulse sequences. For both CODE and rGRE, $BW = SW$ = 80 kHz, n_{acq} = 128, and n_{short} = 4. In CODE, the duration of the sinc pulse ($T_{p,sinc}$) was set to be 100 μs. With the same B_1^{max} value used with the sinc pulse, the duration of the square pulse ($T_{p,square}$) is 21.67 μs. In the case of equal SAR produced by sinc and square

pulses, $T_{p,square}$ = 62.07 μs. The minimum *TE* and *TR* values that could be achieved with CODE were 0.188 ms and 1.877 ms, respectively, for *FOV* = 25 cm, and they were 0.155 ms and 1.811 ms for *FOV* = 40 cm. In the case of the same B_1^{max}, the minimum *TE* and *TR* achievable with rGRE were 0.217 ms and 1.821 ms, respectively, for *FOV* = 25 cm, and 0.172 ms and 1.759 ms for *FOV* = 40 cm. In the case of the same SAR, these were 0.238 ms and 1.863 ms, respectively, for *FOV* = 25 cm, and 0.193 ms and 1.801 ms for *FOV* = 40 cm. In both cases, as compared with rGRE, CODE has a slightly shorter minimum *TE* and slightly longer minimum *TR*. The minimum *TE* and *TR* decreases as *FOV* increases due to the reduction of τ_{ss}, τ_{ro}, and τ_{dephs}.

EXPERIMENTS

CODE and rGRE sequences were implemented and tested on a clinical 3T MAGNETOM Trio scanner (Siemens, Erlangen, Germany), with a 40 mT/m maximum peak gradient amplitude and a 170 mT/m/ms maximum slew rate. The rGRE and CODE sequence codes were written in-house. In all cases of CODE imaging, a tailored sinc pulse available in the Siemens pulse-shape library was used. This tailored sinc pulse delivers a very flat excitation profile in the pulse bandwidth. A 12-element head coil (Siemens “Head Matrix”) for signal reception in combination with a transmit body coil was used for imaging the resolution phantom. *In vivo* human knee images were acquired with a transmit/receive birdcage knee coil (Siemens “CP Extremity”). Imaging of normal human volunteers was performed according to the procedure approved by the Institutional Review Board of the University of Minnesota Medical School. For offline image reconstruction, gridding was performed onto two-times oversampled Cartesian grid using a Kaiser-Bessel interpolation kernel with a diameter of 4. No additional corrections were applied to compensate for gradient timing errors and non-linearity, which, however, does not imply that CODE is robust to gradient delays.

Imaging of a resolution phantom (Nuclear Associates 76-903, Fluke Biomedical) was performed to assess the relative image quality and performance of the two sequences. In Fig. 4, phantom images are shown in axial (a and b) and sagittal (c and d) planes. Signal intensity (SI) profiles are also shown along the white solid line in the sagittal images obtained with rGRE (e) and CODE (f), respectively. In all cases, flip angle = 5°, *TR* = 3.4 ms, *FOV* (= *THK*) = 30 cm, and number of projections = 128 k, to achieve 1.0 mm^3 isotropic resolution in a scan time of ~6 min. rGRE was performed with *TE* = 0.22 ms and $T_{p,square}$ = 0.05 ms. CODE was performed with *TE* = 0.19 ms and a sinc pulse of duration 0.1 ms (= $T_{p,sinc}$) and *R* = 6.4.

In vivo human knee imaging was also performed using CODE with the shortest *TE*, i.e., *TE* = 0.23 ms, which could be practically attained with the 3T Siemens Trio system, when *FOV* = 25 cm. Fat suppression was performed by applying a spectrally-selective suppression pulse after every 32 acquisitions. A sinc pulse with *R* = 10 was used for spin excitation. Other parameters were: $T_{p,sinc}$ = 0.1 ms, flip angle = 4°, and *TE* = 0.23 ms. The number of projections was 100 k, yielding 0.65 mm^3 isotropic resolution in a scan time of ~5 min. To illustrate the general quantity of the 3D imaging, Fig. 5a displays a CODE knee image in an axial view at the level of the patellofemoral joint, which includes anatomical structures such as the patella, femoral lateral and medial trochlear groove articular cartilage, femur, and anterior cruciate ligament insertion at the lateral femoral condyle, along the left-to-right direction. It is worthwhile to note that with a closer look some blurry shades around the knee can be recognized (Fig. 5a, white arrows) which arise from foam pads used to restrict knee movement. These pads, which are in the gap between the knee and the knee coil, are more clearly seen with slice averaging. In Fig. 5b, twenty slices were averaged around the slice shown in Fig. 5a and the averaged image was rescaled for better visualization of the foam

padding. While signals from the foam padding are not usually visible with conventional MRI sequences, Fig. 5b illustrates that special attention should be paid to the choice of materials used for supporting structures within the FOV when using ultrashort *TE* imaging, even when using only modestly short *TE* of ~0.2 ms.

Sagittal images of *in vivo* human knee acquired using CODE with *TE* = (a) 0.5 ms and (b) 1.0 ms are shown in Fig. 6. A sinc pulse with $T_{p,sinc}$ = 0.25 ms and R = 12.7 was used for spin excitation. Other parameters were: flip angle = 4°, *TR* = 4 ms, and *FOV* (= slab width) = 25 cm. The number of projections was 128 k, yielding = 0.91 mm^3 isotropic resolution in a scan time of ~8 min. Fat suppression was also performed using a spectrally-selective suppression pulse after every 32 acquisitions. With both *TE* values, CODE provided good sensitivity to visualize connective tissues with a majority of short T_2 components, such as cartilage, anterior and posterior horn medial menisci, patellar tendon, and anterior and posterior cruciate ligament. Although fat signals were generally well suppressed, signals from fatty tissues increased as *TE* decreased. This may be due to an increasing contribution of short T_2 signal components from fatty tissue as *TE* decreases.

DISCUSSION AND CONCLUSIONS

The most appealing feature of the two 3D radial GRE sequences described here (rGRE and CODE) is their readiness for implementation on standard clinical MR systems, apparently without placing stringent or unique demands on hardware performance. As shown in this work, these techniques can attain relatively short *TE* and *TR* despite the limitations of peak RF power, transmit/receive switching time, coil ring down time, and slew rate that are typical for a standard 3 T clinical scanner. These radial GRE sequences can avoid some of the technical challenges arising from non-uniform sampling that conventional UTE imaging encounters, since data sampling occurs after the gradient has reached a stable plateau. An advantage of 3D MRI is the ability to obtain high-resolution images without missing any information between slices, but 3D MRI has the disadvantage of typically requiring a much longer scan time than 2D imaging. In the case of these radial imaging techniques, however, there are potential ways of reducing the scan time which were not exploited here, e.g., by under-sampling projection trajectories (16,17). In principle, with radial acquisitions, the number of projections, which determines the scan time, does not affect the spatial resolution, but rather affects the size of artifact-free zone.

The CODE sequence has the unique feature that the dephasing lobe of the readout gradient is applied during RF excitation. Such an application of the initial dephasing (or pre-dephasing) gradient during RF excitation enables CODE to offer a much shorter *TE* than conventional GRE methods and ~15% shorter *TE* than the rGRE sequence employing a short square pulse. Here it was shown that *TE* ≥ ~0.2 ms can be achieved in high resolution 3D imaging with a 3T clinical scanner. For example, the achievable shortest *TE* is 0.22 ms and 0.18 ms for *FOV* = 25 cm and 40 cm, respectively, as shown in Table 1. Although the theoretically expected minimum *TE* is 0.19 ms and 0.16 ms for *FOV* = 25 cm and 40 cm, respectively (Table 2), the shortest *TE* values that could be attained in this practical setting with a standard clinical scanner are 20 – 30 μs longer than the theoretically expected ones due to some hardware limitations and/or the automatic hardware synchronization inside the system designed to eliminate possible timing errors.

Limitations in CODE

In CODE, a frequency-selective pulse with a very short pulse duration (e.g., a sinc with T_p = 0.1 – 0.2 ms) is used for reducing *TE*, and thus, a flip-angle restriction is put on CODE. In other words, CODE may be unable to attain large flip angles, i.e., flip angles larger than ~10°, due to the peak B_1 or SAR limitation (Table 1). Thus, although a certain degree of T_1-

weighting is possible, extreme T_1-weighted imaging cannot be achieved in human applications with CODE when the shortest *TE* is desired. Of course, a larger flip angle can also be attained in CODE by increasing T_p at the cost of a longer *TE*. In this case, *TE* should be increased by the amount of increase in $T_p/2$ provided that other parameters remain the same.

Because a frequency-selective pulse is used for excitation in CODE, the initial dephasing gradient for readout must also serve as a slab-selective gradient during excitation. However, strictly speaking, the "real" slab selection does not work for CODE, since it is based on a radial acquisition scheme. In other words, the slab excitation inside an object along a specific direction is not currently feasible because the orientation of the slab changes with every projection. For the same reason, it is also challenging to image a selected region-of-interest (ROI) inside an object by using this slab selection. Recently, ROI reconstruction from limited-angle local projection data, which is called interior reconstruction, was proposed for computed tomography (18,19) and provided the promising possibility that it is applicable to MRI with radial sampling (20). However, the current version of CODE can only be applied to 3D MRI without limiting the FOV by slab selection, and thus, in every direction the excited slab width should exceed the dimensions of the object, unless the sensitive volume is bounded by the sensitivity profile(s) of the local receiver coil(s).

Although CODE cannot attain a *TE* much less than ~0.2 ms with current clinical scanners, it can be applied to a variety of musculoskeletal studies. Connective tissues, such as meniscus, tendons, ligaments, and cortical bone, contain predominantly bound water with short T_2 values on the order of a few hundreds of microseconds to a few milliseconds (21-23). As demonstrated in the musculoskeletal system in this paper, CODE offers a combination of high SNR with the ability to create differential contrast between tissues dominated by short T_2 components. The images reveal details such as the parallel orientation of the quadriceps tendon fiber bundles, the medial menisci, and the anterior and posterior cruciate ligament. CODE is also potentially useful for dynamic contrast enhanced (DCE) MRI studies at high magnetic fields, since it can effectively reduce T_2*-weighting or signal loss which distorts the time-intensity curve and thus leads to erroneous estimates of pharmacokinetic parameters (24).

This study shows that 3D radial GRE sequences such as rGRE and CODE have the capability of permitting *TE* as short as ~0.2 ms using a standard clinical scanner. This range of *TE* is not shorter than that possible with UTE, SWIFT, and WASPI, but it might be sufficient for many types of MRI studies of short T_2 signals. Considering the straightforward implementation and the apparent robustness of these 3D radial GRE sequences, they appear to be promising alternatives to other ultrashort T_2 sequences in certain cases.

Acknowledgments

This research was supported by NIH grant P41 RR008079. This work was also supported by National Research Foundation of Korea (NRF) funded by Ministry of Education, Science, and Technology (No. 2010-0025744).

Grant Sponsors: NIH Grants P41 RR008079, NRF Grants No. 2010-0025744

Symbols

$\boldsymbol{G_{ro}}$	Italic Roman upper case 'gee' with subscript Roman lower cases 'ro'
$\boldsymbol{G_{ss}}$	Italic Roman upper case 'gee' with subscript Roman lower cases 'ss'
$\boldsymbol{\tau}$	Greek lower case 'tau'

T_{p}	Italic Roman upper case ‘tee’ with subscript Roman lower case ‘pee’
T_{acq}	Italic Roman upper case ‘tee’ with subscript Roman lower cases ‘acq’
THK	Italic Roman upper cases ‘THK’
THK	Italic Roman upper cases ‘FOV’
BW	Italic Roman upper cases ‘BW’
SW	Italic Roman upper cases ‘SW’
γ	Greek lower case ‘gamma’
TE_{CODE}	Italic Roman upper cases ‘TE’ with subscript Roman upper cases ‘CODE’
τ_{ss}	Italic Greek lower case ‘tau’ with subscript Roman lower cases ‘ss’
τ_{ro}	Italic Greek lower case ‘tau’ with subscript Roman lower cases ‘ro’
τ_{ext}	Italic Greek lower case ‘tau’ with subscript Roman lower cases ‘ext’
T_{short}	Italic Roman upper case ‘tee’ with subscript Roman lower cases ‘short’
SR	Italic Roman upper cases ‘SR’
TE_{1}	Italic Roman upper case ‘TE’ with subscript ‘one’
TE_{2}	Italic Roman upper case ‘TE’ with subscript ‘two’
$\tau_{ss,1}$	Italic Greek lower case ‘tau’ with subscript Roman lower cases ‘ss’, coma symbol, ‘one’
$\tau_{ss,2}$	Italic Greek lower case ‘tau’ with subscript Roman lower cases ‘ss’, coma symbol, ‘two’
$T_{short,1}$	Italic Roman upper case ‘tee’ with subscript Roman lower cases ‘short’, coma symbol, one’
$T_{short,2}$	Italic Roman upper case ‘tee’ with subscript Roman lower cases ‘short’, coma symbol, ‘two’
BW_{1}	Italic Roman upper case ‘BW’ with subscript ‘one’
BW_{2}	Italic Roman upper case ‘BW’ with subscript ‘two’
$G_{ss,1}$	Italic Roman upper case ‘gee’ with subscript Roman lower cases ‘ss’, coma symbol, ‘one’
$G_{ss,2}$	Italic Roman upper case ‘gee’ with subscript Roman lower cases ‘ss’, coma symbol, ‘two’
TR_{CODE}	Italic Roman upper cases ‘TR’ with subscript Roman upper cases ‘CODE’
n_{acq}	Italic Roman lower case ‘en’ with subscript Roman lower cases ‘acq’
n_{short}	Italic Roman lower case ‘en’ with subscript Roman lower cases ‘short’
R	Italic Roman upper cases ‘aal’
G_{deph}	Italic Roman upper case ‘gee’ with subscript Roman lower cases ‘deph’
TE_{rGRE}	Italic Roman upper cases ‘TE’ with subscript Roman lower case ‘aal’, Roman upper cases ‘GRE’
τ_{deph}	Italic Greek lower case ‘tau’ with subscript Roman lower cases ‘deph’

TR_{rGRE}	Italic Roman upper cases ‘TR’ with subscript Roman lower case ‘aal’, Roman upper cases ‘GRE’
B_1	Italic upper case ‘bee’ with subscript ‘one’
c	Italic Roman lower cases ‘see’
A_{deph}	Italic Roman upper case ‘ei’ with subscript Roman lower cases ‘deph’
A_{reph}	Italic Roman upper case ‘ei’ with subscript Roman lower cases ‘reph’
π	Greek lower case ‘pi’
$T_{p,sinc}$	Italic Roman upper case ‘tee’ with subscript Roman lower case ‘pee’, coma symbol, Roman lower cases ‘sinc’
$T_{p,square}$	Italic Roman upper case ‘tee’ with subscript Roman lower case ‘pee’, coma symbol, Roman lower cases ‘square’

REFERENCES

1. Pauly JM, Conolly SM, Nishimura DG, Macovski A. Slice-selective excitation for very short T_2 species. in 8th Annual Meeting of the International Society of Magnetic Resonance in Medicine. Amsterdam. 1989:28.
2. Glover GH, Pauly JM, Bradshaw KM. Boron-11 imaging with a three dimensional reconstruction method. J Magn Reson Imaging. 1992; 2:47–52. [PubMed: 1623280]
3. Idiyatullin D, Corum C, Park J-Y, Garwood M. Fast and quiet MRI using a swept radiofrequency. J Magn Reson. 2006; 181:342–349. [PubMed: 16782371]
4. Idiyatullin D, Corum C, Moeller S, Garwood M. Gapped pulses for frequency-swept MRI. J Magn Reson. 2008; 193:267–273. [PubMed: 18554969]
5. Rahmer J, Bornert P, Groen J, Bos C. Three-dimensional radial ultrashort echo-time imaging with T_2 adapted sampling. Magn Reson Med. 2006; 55:1075–1082. [PubMed: 16538604]
6. Brittain JH, Shankaranarayanan A, Ramanan AV, Shimakawa A, Cunningham CH, Hinks RS, Francis IR, Turner R, Johnson J, Nayak KS, Tan SG, Pauly JM, Bydder GM. Ultrashort TE imaging with single-digit (8μs) TE. in 12th Annual Meeting of the International Society of Magnetic Resonance in Medicine. Kyoto. 2004:629.
7. Tyler DJ, Robson MD, Henkelman RM, Young IR, Bydder GM. Magnetic resonance imaging with ultrashort TE (UTE) pulse sequences: Technical considerations. J Magn Reson Imaging. 2007; 25:279–289. [PubMed: 17260388]
8. Wu Y, Ackerman JL, Chesler DA, Graham L, Wang Y, Glimcher MJ. Density of organic matrix of native mineralized bone measured by water- and fat-suppressed proton projection. MRI Magn Reson Med. 2003; 50:59–68.
9. Madio DP, Lowe IJ. Ultra-fast imaging suing low flip angles and FIDs. Magn Reson Med. 1995; 34:525–529. [PubMed: 8524019]
10. Tsao J, Behnia B, Webb AG. Unifying linear prior-information-driven methods for accelerated image acquisition. Magn Reson Med. 2001; 46:652–660. [PubMed: 11590640]
11. Kuethe DO, Caprihan A, Lowe IJ, Madio DP, Gach MH. Transforming NMR data despite missing points. J Magn Reson. 1999; 139:18–25. [PubMed: 10388580]
12. Hsu J-J, Lowe IJ. Signal recovery in free induction decay imaging using a stimulated echo. Magn Reson Med. 2002; 47:409–414. [PubMed: 11810688]
13. Kuethe DO, Adolphi NL, Fukushima E. Short data-acquisition times improve projection images of lung tissue. Magn Reson Med. 2007; 57:1058–1064. [PubMed: 17534926]
14. Wong STS, Roos MS. A strategy for sampling on a sphere applied to 3D selective RF pulse design. Magn Reson Med. 1994; 32:778–784. [PubMed: 7869901]
15. Pipe JG, Menon P. Sampling density compensation in MRI: Rationale and an iterative numerical solution. Magn Reson Med. 1999; 41:179–186. [PubMed: 10025627]

16. Peters DC, Korosec FR, Grist TM, Block WF, Holden JE, Vigen KK, Mistretta CA. Undersampled projection reconstruction applied to MR angiography. Magn Reson Med. 2000; 43:91–101. [PubMed: 10642735]

17. Barger AV, Block WF, Toropov Y, Grist TM, Mistretta CA. Time-resolved contrast-enhanced imaging with isotropic resolution and broad coverage using an undersampled 3D projection trajectory. Magn Reson Med. 2002; 48:297–305. [PubMed: 12210938]

18. Ye Y, Yu H, Wang G. Exact interior reconstruction with cone-beam CT. Int J Biomed Eng. 2007 ID 10693:5 pages.

19. Ye Y, Yu H, Wang G. Exact interior reconstruction from truncated limited-angle projection data. Int J Biomed Eng. 2008 ID 427989:6 pages.

20. Zhang J, Yu H, Corum C, Garwood M, Wang Ge. Exact and stable interior ROI reconstruction for radial MRI. Medical Imaging 2009: Physics of Medical imaging. Proc. of SPIE. 7258:72585G.

21. Gold GE, Thedens DR, Pauly JM, Fechner KP, Bergman G, Beaulieu CF, Macovski A. MR imaging of articular cartilage of the knee: new methods using ultrashort TEs. Am J Roentgenol. 1998; 170:1223–1226. [PubMed: 9574589]

22. Gatehouse PD, Thomas RW, Robson MD, Hamilton G, Herlihy AH, Bydder GM. Magnetic resonance imaging of the knee with ultrashort TE pulse sequences. Magn Reson Img. 2004; 22:1061–1067.

23. Reichert ILH, Robson MD, Gatehouse PD, He T, Chappell KE, Holmes J, Girgis S, Bydder G. Magnetic resonance imaging of cortical bone with ultrashort TE pulse sequences. Magn Reson Img. 2005; 23:611–618.

24. de Bazelaire C, Rofsky NM, Duhamel G, Zhang J, Michaelson MD. Combined T_2* and T_1 measurements for improved perfusion and permeability studies in high field using dynamic contrast enhancement. Eur Radiol. 2006; 16:2083–2091. [PubMed: 16583215]

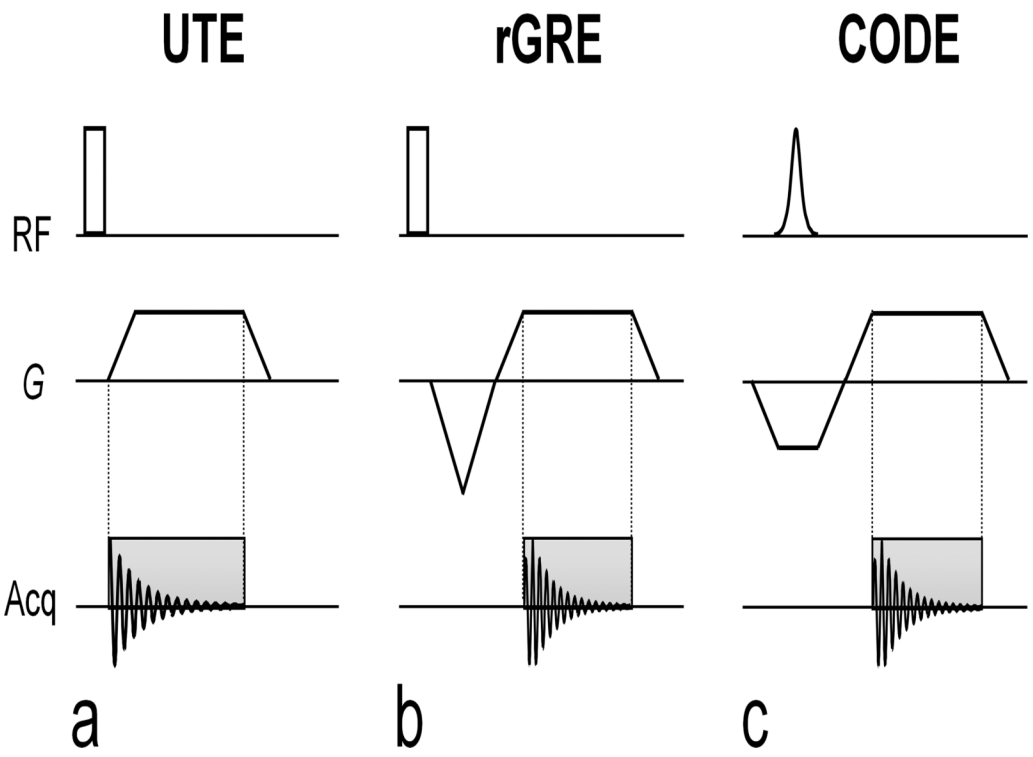

FIG. 1.

Pulse sequence diagrams of 3D UTE, 3D radial GRE (rGRE), and CODE. (a) In the 3D UTE, a square pulse is used for spin excitation and data acquisition starts during the readout gradient ramp to achieve the shortest acquisition delay possible. Since no dephasing gradient is applied for readout, a FID is acquired during acquisition. (b) In rGRE, a square pulse is also used for excitation. Data is acquired during the readout gradient following an initial dephasing (or pre-dephasing) gradient, and thus, a gradient echo is acquired instead of the FID. A partial gradient-echo acquisition scheme is employed to minimize *TE*. (c) In CODE, slab selection and pre-dephasing are performed with the same gradient. In other words, a pre-dephasing gradient is applied during, not after, spin excitation. Hence, a gradient echo is acquired as in rGRE. A slab-selective pulse such as a sinc or a hyperbolic secant pulse can be used for spin excitation. Because the acquisition time will usually be much longer than the pulse duration (i.e. T_{acq} is on the order of a few milliseconds or less, whereas T_p is usually ~100 – 300 microseconds), the peak of the gradient echo forms soon after the start of the acquisition period and, thus, the gradient echoes used to fill *k*-space in each radial direction are asymmetric about the origin of *k*-space.

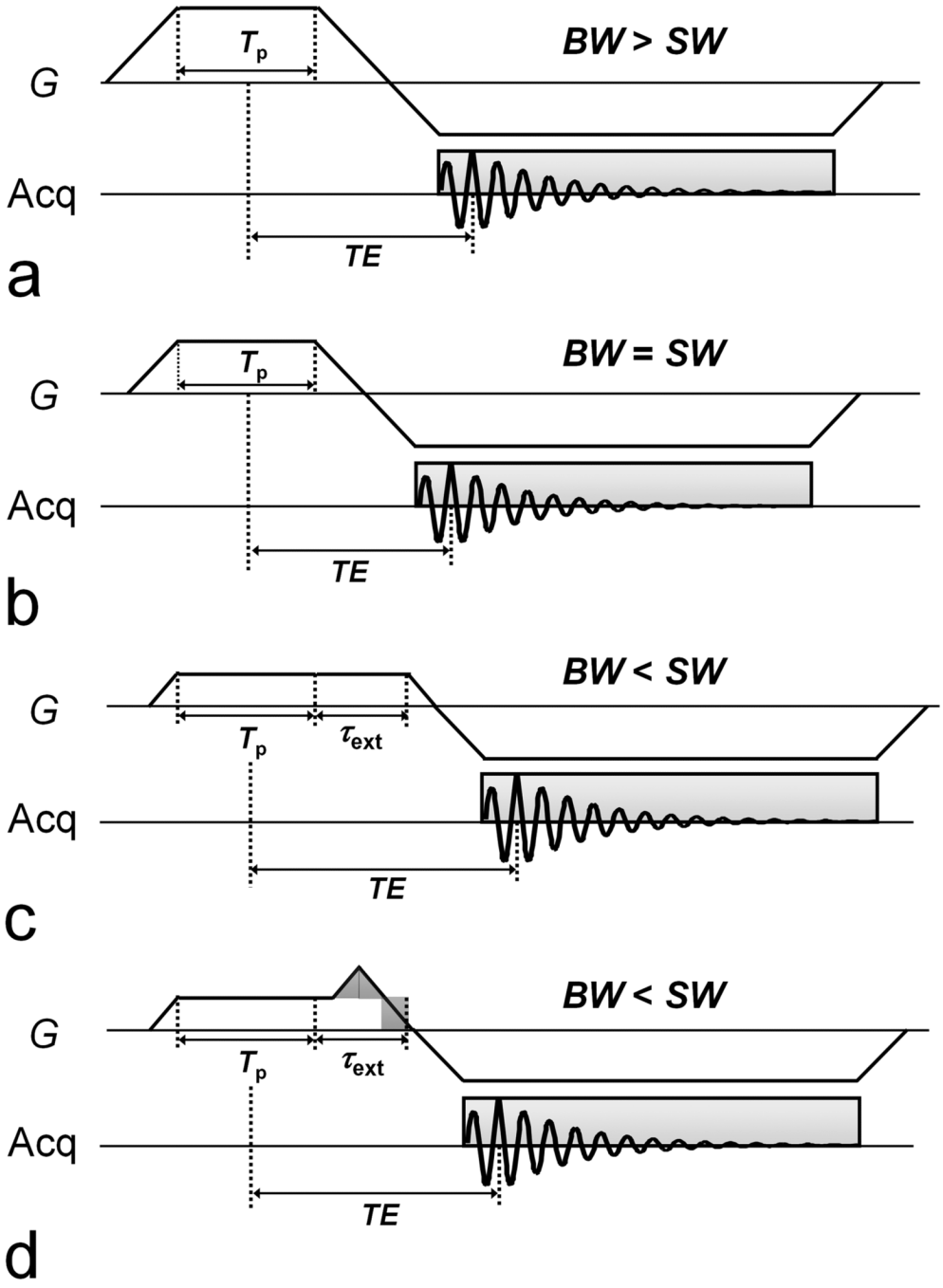

FIG. 2.

Pulse sequence diagrams of CODE for three different situations, i.e., $BW > SW$ (or $G_{ss} > G_{ro}$), $BW = SW$ (or $G_{ss} = G_{ro}$), and $BW < SW$ (or $G_{ss} < G_{ro}$), which are referred to as case 1 (a), case 2 (b), and case 3, respectively. Particularly in case 3, the gradient area for the pre-dephasing is less than that for the readout, and as a result additional time for dephasing with G_{ss} is needed to keep the echo peak from occurring during the readout gradient ramp. Two sequence schemes are possible for this purpose. In the case of the basic scheme (c), which is referred to as case 3a, G_{ss} is simply extended having the same constant value as the original setup. However, in case 3b (d), a part of the extended gradient is replaced with gradient ramps (i.e., ramp-up and ramp-down) with an area (shaded triangle) equal to that of a part of

the extended gradient to be replaced (shaded rectangle). The latter always provides a shorter *TE* than the former by the amount of time corresponding to the width of the shaded rectangle. As proven herein (see text), case 2 provides the shortest *TE* among the possible schemes, except in some specific circumstances (e.g., small *FOV*), case 3b provides the shortest *TE*.

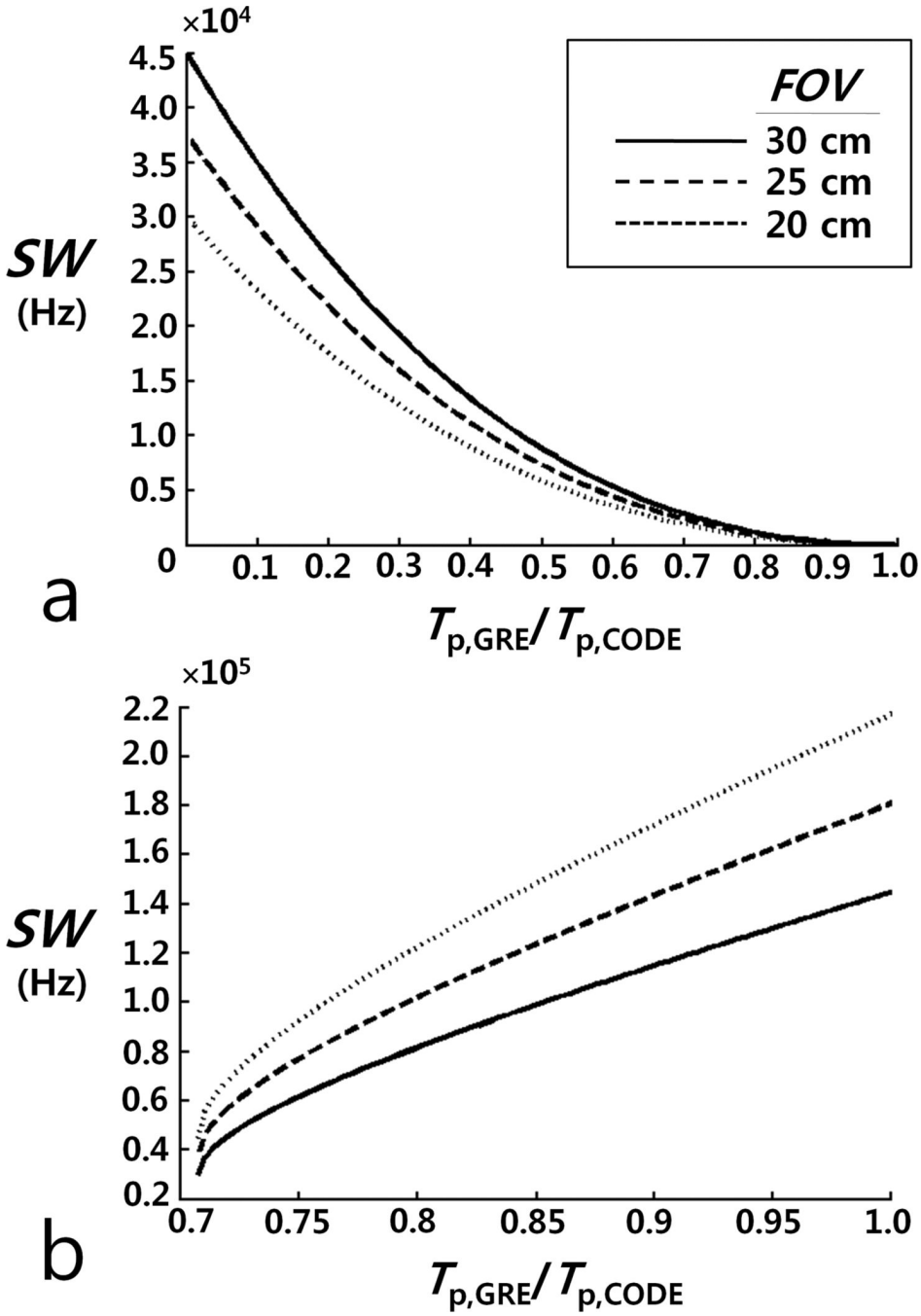

FIG. 3.

Plots showing the relationship between *SW* and the ratio of the pulse length ($T_{p,GRE}$) in rGRE to the pulse length ($T_{p,CODE}$) in CODE for different *FOV*s = 20, 25, and 30 cm, (a) when the achievable minimum *TE* of CODE is equal to that of rGRE and (b) when the achievable minimum *TR* of CODE is equal to that of rGRE. (a) For a given $T_{p,GRE}/T_{p,CODE}$, CODE provides a shorter *TE* than rGRE if *SW* is larger than the plotted value. (b) While CODE has a longer *TR* than rGRE for $T_{p,GRE}/T_{p,CODE} < 0.7071$, it has a shorter *TR* than rGRE for $T_{p,GRE}/T_{p,CODE} \geq 0.7071$, provided that *SW* is smaller than the plotted value.

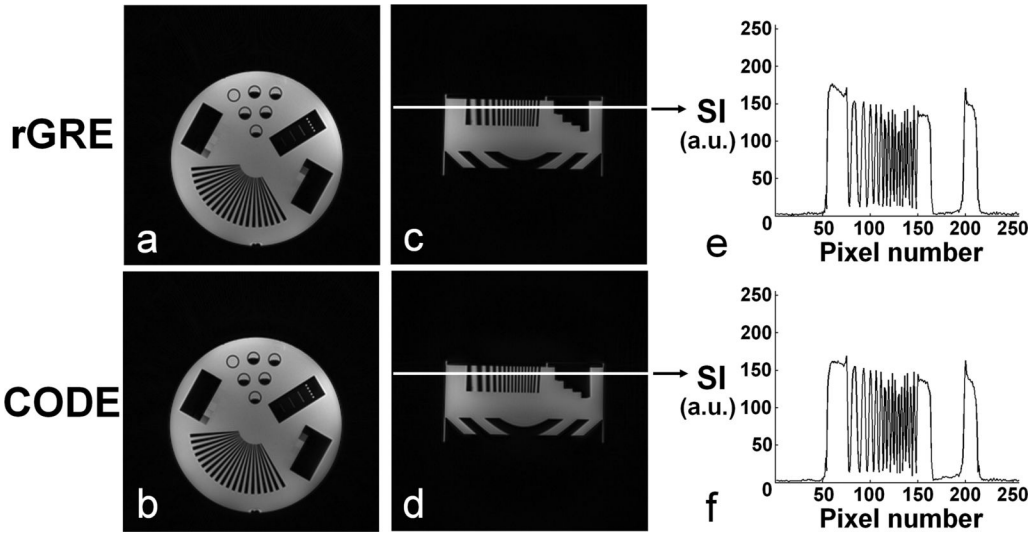

FIG. 4.

Resolution phantom images acquired using rGRE and CODE. Phantom images are shown in axial (a and b) and sagittal (c and d) planes. Signal intensity (SI) profiles are also shown along the white solid line in the sagittal images obtained with rGRE (e) and CODE (f), respectively. In all cases, flip angle = 5°, *TR* = 3.4 ms, and *FOV* (= slab width) = 30 cm. The number of projections = 128 k. Scan time = ~6 min. Isotropic resolution = 1.0 mm^3. For 3D radial GRE images (a and c), a square pulse was used with $T_{p,square}$ = 0.05 ms and *TE* = 0.22 ms. For CODE images (b and d), a sinc pulse was used with $T_{p,sinc}$ = 0.1 ms and *TE* = 0.19 ms.

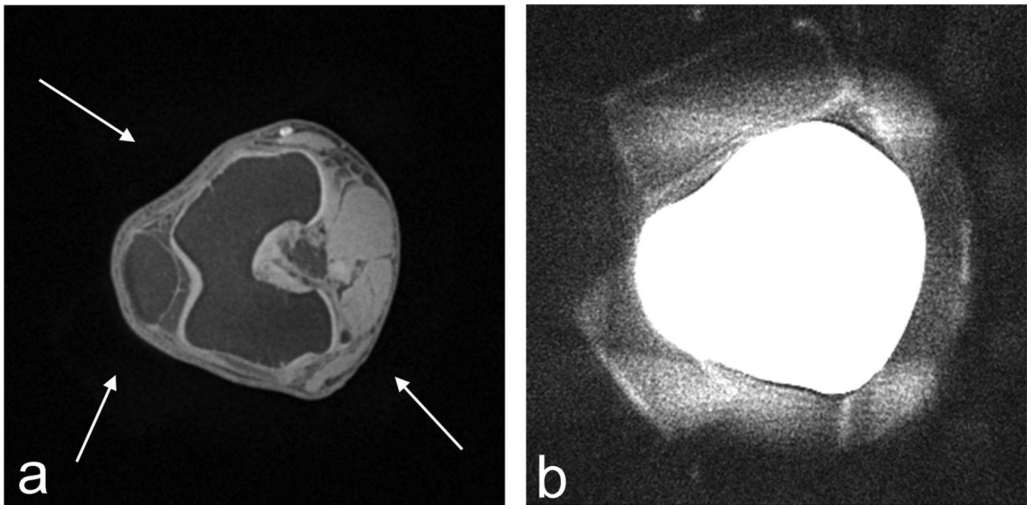

FIG. 5.

(a) Axial image and (b) slice-averaged and rescaled image of *in vivo* human knee acquired using CODE with *TE* = 0.23 ms. $T_{p,sinc}$ = 0.1 ms, flip angle = 4°, *FOV* (= *THK*) = 25 cm, isotropic resolution = 0.65 mm^3, and scan time = ~5 min. In (a), an axial knee image was chosen at the level of the patellofemoral joint among the 3D data set, showing an anatomical structure such as the patellar, the femoral lateral and medial trochlear groove articular cartilage, the femur, and the anterior cruciate ligament insertion at the lateral femoral condyle, along the left-to-right direction in the slice. With a closer look, some blurry shades around the knee can be recognized in (a), which are pointed to (white arrows). These signals arise from the foam pads placed between the knee and coil to minimize motion artifacts. These pads are more clearly seen in the image shown in (b) which was obtained by averaging 20 adjacent slices and adjusting the image intensity.

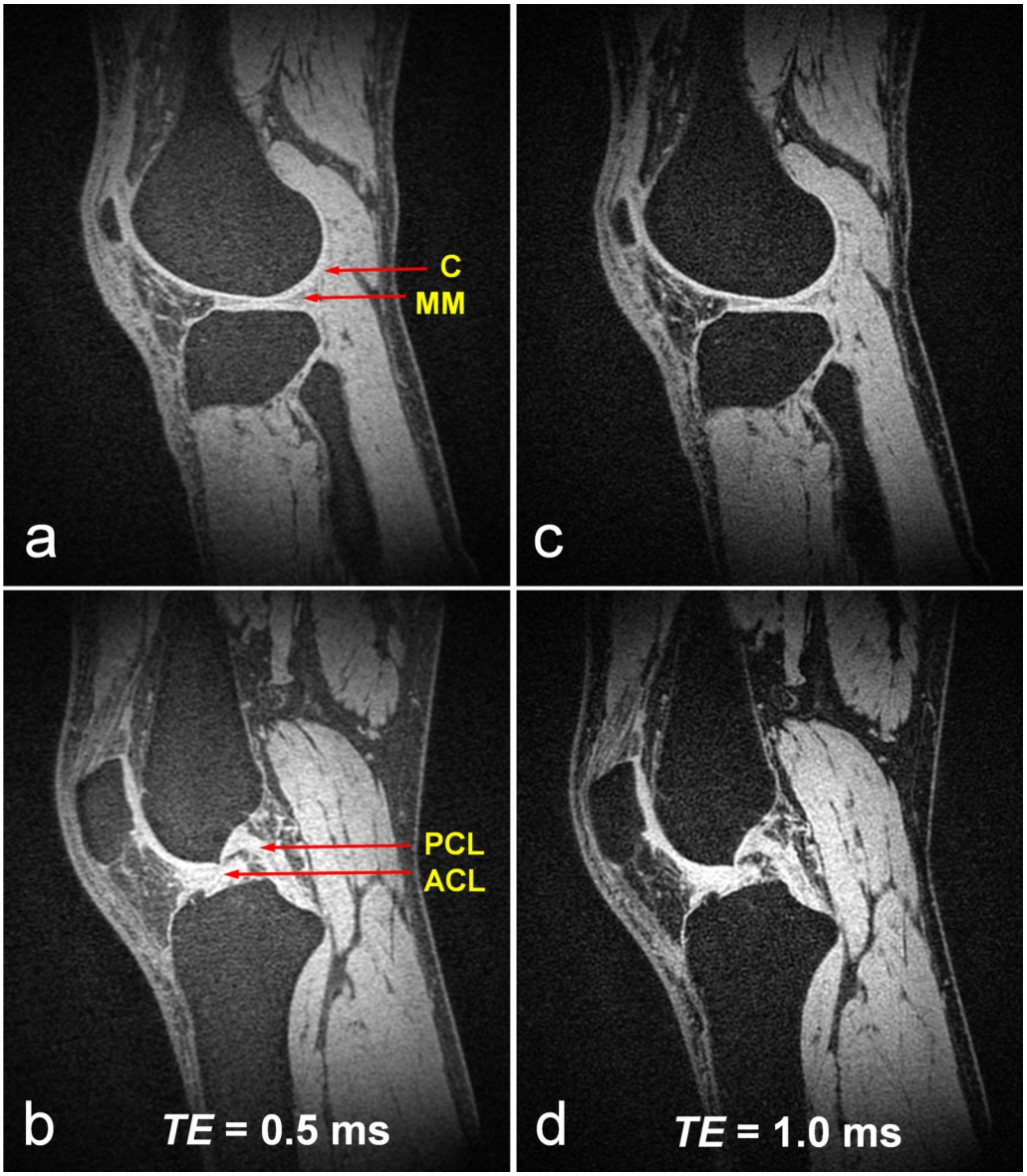

FIG. 6.

Sagittal images of *in vivo* human knee acquired using CODE with different echo times, i.e., *TE* = 0.5 ms in (a) and (b), *TE* = 1.0 ms in (c) and (d). $T_{p,sinc}$ = 0.25 ms, flip angle = 4°. *TR* = 4 ms, and *FOV* (= slab width) = 25 cm. The number of projections = 128 k. Scan time = ~8 min. Isotropic resolution = 0.91 mm^3. Fat suppression was performed using a spectral-selective suppression pulse after every 32 acquisitions. With both *TE* values, CODE provides good sensitivity for visualizing connective tissues with a majority of short T_2 components, such as cartilage (C) (a, c), anterior and posterior horn medial menisci (MM) (a, c), patellar tendon (a ~ d), and anterior and posterior cruciate ligament (ACL and PCL) (b, d). Despite good suppression of fat signals, signals from fatty tissues increased as *TE* decreased, which may be due to the increasing contribution of the short T_2 components of fatty tissue.

Table 1

The minimum *TE* and maximum flip angles achieved with CODE on a 3T MAGNETOM Trio scanner, using a sinc pulse with $R = 10$.

	FOV (cm)	Pulse length (ms)	Min *TE* (ms)	Max flip angle (degree)
Knee coil	25	0.10	0.22	6
		0.15	0.26	9
		0.20	0.29	11
		0.25	0.31	12
	40	0.10	0.18	6
		0.15	0.22	9
		0.20	0.25	11
		0.25	0.27	12
Body coil	25	0.10	0.22	3
		0.15	0.26	5
		0.20	0.29	6
		0.25	0.31	9
	40	0.10	0.18	3
		0.15	0.22	5
		0.20	0.25	6
		0.25	0.27	9

*MAGNETOM Trio scanner, using a sinc pulse with $R = 10$.

Table 2

The minimum *TE* and *TR* (in ms) theoretically achievable with CODE and rGRE.

FOV		CODE	rGRE	
			same B_{1max}	same SAR
25 cm	TE_{min}	0.188	0.217	0.238
	TR_{min}	1.847	1.821	1.863
40 cm	TE_{min}	0.155	0.172	0.193
	TR_{min}	1.811	1.759	1.801

*Assumes slew rate of 3T Siemens MAGNETOM Trio scanner (170 mT/m/ms)